WILEY | Hindawi

Research Article

Homotopic Solution for 3D Darcy–Forchheimer Flow of Prandtl Fluid through Bidirectional Extending Surface with Cattaneo–Christov Heat and Mass Flux Model

Shamaila Batool,[1] A. M. Alotaibi,[2] Waris Khan [iD],[3] Ahmed Hussein Msmali [iD],[4] Ikramullah [iD],[5] and Wali Khan Mashwani [iD][1]

[1]Institute of Numerical Sciences, Kohat University of Science and Technology, Kohat, Pakistan
[2]Department of Mathematics, Faculty of Science, University of Tabuk, P.O. Box 741, Tabuk 71491, Saudi Arabia
[3]Department of Mathematics and Statistics, Hazara University, Mansehra, KP, Pakistan
[4]Department of Mathematics, Collage of Science, Jazan University, Jizan, Saudi Arabia
[5]Department of Physics, Kohat University of Science and Technology, Kohat 26000, Khyber Pakhtunkhwa, Pakistan

Correspondence should be addressed to Wali Khan Mashwani; mashwanigr8@gmail.com

The 3D Prandtl fluid flow through a bidirectional extending surface is analytically investigated. Cattaneo–Christov fluid model is employed to govern the heat and mass flux during fluid motion. The Prandtl fluid motion is mathematically modeled using the law of conservations of mass, momentum, and energy. The set of coupled nonlinear PDEs is converted to ODEs by employing appropriate similarity relations. The system of coupled ODEs is analytically solved using the well-established mathematical technique of HAM. The impacts of various physical parameters over the fluid state variables are investigated by displaying their corresponding plots. The augmenting Prandtl parameter enhances the fluid velocity and reduces the temperature and concentration of the fluid. The momentum boundary layer boosts while the thermal boundary layer mitigates with the rising elastic parameter (α_2) strength. Furthermore, the enhancing thermal relaxation parameter (γ_e)) reduces the temperature distribution, whereas the augmenting concentration parameter (γ_c) drops the strength of the concentration profile. The increasing Prandtl parameter declines the fluid temperature while the augmenting Schmidt number drops the fluid concentration. The comparison of the HAM technique with the numerical solution shows an excellent agreement and hence ascertains the accuracy of the applied analytical technique. This work finds applications in numerous fields involving the flow of non-Newtonian fluids.

1. Introduction

Non-Newtonian fluids are those fluids that do not obey Newton's law of fluid motion. The Newtonian fluids have constant viscosity as evidenced by the direct relationship between the shear stress and the resulting strain. The majority of applications of non-Newtonian fluids in different fields such as petroleum production, bio-chemicals preparation, pharmaceutical industry, food, and power engineering, have been thoroughly investigated by various researchers and investigators. The non-Newtonian fluids, for example, genetic and manufactured liquid organisms, polymers, emulsions, paints, blood, oil, toothpaste, and ketchup, have a crucial and important role in this advanced scientific, industrial, and technological arena. The non-Newtonian fluids due to their complex and nonlinear nature are very difficult to be handled both numerically as well as analytically as compared to Newtonian fluids. Carreau [1, 2] for the first time introduced an expression for the stress tensor that models the nonlinear and viscoelastic features of

non-Newtonian fluids. The Carreau relation for the stress tensor has opened the way to investigate the non-Newtonian fluids both analytically and numerically.

Non-Newtonian fluids may be further divided into many types based on their physical characteristics. There exists an important type called shear thinning or pseudoplastic fluids. The viscosity of such fluids displays a decreasing tendency to the applied shear stress. The most important and common example of such kind of fluid is the human blood. Researchers have developed different models to describe the behavior and properties of shear-thinning fluids. The importance of these models is the Prandtl fluid model, which is capable to describe the shear-thinning nature of such kinds of fluids. Akbar et al. [3] inspected the outcomes of hydromagnetic stagnation-point flow of Prandtl fluid through stretching flat surface embedded in a porous medium. Bilal et al. [4] analyzed the consequences of double diffusion on the MHD Prandtl nanoliquid moving through an extended sheet taking into account the effects of external magnetic influence. Nadeem et al. [5] performed the analytical treatment of a Prandtl fluid model with heat transfer characteristics. Khan et al. [6] briefly investigated the impacts of homogenous and heterogeneous reactions on the 2D MHD flow of Prandtl fluid through a nonlinear heated surface. Amanullah et al. [7] investigated the hydromagnetic flow of Prandtl-Eyring fluid through an isothermal permeable spherical surface, considering the magnetic and slip effects. The effect of slip-on electrically conductive hydromagnetic boundary layer flow through an exponentially extended sheet with viscous dissipation and thermal radiation has been investigated by Mukhopadhyay [8]. Ali et al. [9] described the unique features of unsteady Eyring-Powell nanofluid flow near the stagnation point through a convectively heated stretching surface. Further relevant studies about viscoelastic Prandtl fluid can be studied in references [10–19]. Abbas et al. [20] addressed the entropy optimized Darcy–Forchheimer nanofluid flow through an elongated curved surface with MHD and temperature-dependent viscosity effects. Sreedevi and Reddy [21] examined the impacts of thermophoresis and Brownian motion on the hydromagnetic 3D Maxwellian nanoliquid migration through a stretching sheet in the presence of thermal radiation and chemical reaction effects. Recently, enormous research on the dynamic features of nanofluid motion has been undertaken in references [22–27].

MHD and electrically conducting flows of non-Newtonian fluids through stretching surfaces have enormous applications in the different fields of engineering and technology. Some of them are hot rolling, glass fiber, nuclear reactor cooling, plastic sheet extrusion, metal casting, glass blowing, and metallurgical casting. Abel et al. [28] analyzed the effects of heat transport and MHD motion over 2D UCM fluid flow through a stretching surface in the presence of induced magnetic parameter. Vishnu et al. [29] performed the Lie symmetry analysis of the magnetic field effects on the free convection nanofluid flow over a semi-infinite stretchable surface. Das et al. [30] demonstrated the hydromagnetic nanofluid flow through a stretching surface embedded in permeable source through a rotating frame.

Ibrahim et al. [31] numerically analyzed the impacts of heat source and applied magnetic field on the mixed convective MHD dissipative Casson nanoliquid stagnation-point flow through a stretching surface by taking into account the convective boundary condition and velocity slip impacts. Kumar et al. [32] thoroughly examined the hydromagnetic flow of chemically reactive non-Newtonian viscoelastic Williamson liquid through a curved/flat sheet with generation of variable heat and radiation effects. Das and Zheng [33] studied the impacts of melting and external magnetic force on the stagnation-point flow of conducting viscoelastic Jeffrey fluid through a curved surface with Newtonian heating. Aziz and Afify [34] evaluated numerically the MHD and boundary layer flow through a curved surface in the presence of magnetic field and viscous dissipation. Recently, Abbas et al. [35] studied 3D MHD flow of micropolar nanofluid through a rotating permeable exponentially elongated surface using convective boundary conditions. In [36–38], homotopy analysis method (HAM) has applied for solving various types of nonlinear differential equations. In [39], the influence of thermal radiation, inclined magnetic field, and stratification on the third-grade nanofluid with swimming gyrotactic microorganisms have been mainly analysed by using the optimal homotopy analysis method (OHAM). The fluid is flowing past a horizontal cylinder exposed to an inclined magnetic field. The boundary layer system of equations is reconstructed into ordinary differential equations using similarity transformations. The system of equations is resolved using the optimal homotopy analysis method (OHAM) and the results are visualized numerically and graphically. The Galerkin finite element scheme has employed for developing new system of equations to investigate the generation of entropy in viscoelastic Sisko nanofluid over a cylinder. The analysis is performed in the existence of nanofluid and motile microorganisms. The magneto-hydrodynamic flow including the inclined magnetic field is considered. Fluxes for heat, mass, the concentration of nano-sized particles, and the concentration of swimming microorganisms are computed and scrutinized [40]. Recently in [41], a simulation model has been employed in order to observe knowledge flow within the regional innovation system under relationships of varying strength. The results show that when the relationship between the subjects of the regional innovation system reaches certain strength, the system will exhibit high module independence and high network integrity, forming a loosely coupled system. The knowledge flow in the system exhibits the emergence of a fast flow rate, a high mean value, and little variance. When relationship strength is at other levels, the emergence of knowledge cannot be identified.

Motivated through the above literature, it is planned to investigate the various thermal features during the three-dimensional Darcy–Forchheimer flow of Prandtl fluid through a stretching and permeable surface. The thermal analysis of the flow is performed using the Cattaneo–Christov model. The main aim of the investigation is to explore the thermal energy transport features of the non-Newtonian Prandtl fluid migrating through a porous and stretching surface. The structure of the article is organized in the following manner.

The geometry and mathematical model of the problem under investigation are presented in Section 2. The model equations are transformed to simple form by using similarity relations. The solution methodology of HAM applied to solve the reduced model is explained in Section 3. The convergence analysis of the applied procedure is discussed in Section 4 by displaying graphs and tables of the state variables. The results are displayed through different graphs describing the impacts of physical parameters over the state functions in Section 5. The work is concluded finally in the last section.

2. Problem Framework

We consider the 3D Darcy–Forchheimer flow of Prandtl fluid through a permeable stretching surface as displayed in Figure 1. The surface temperature and concentration are expected to remain constant. The Cattaneo–Christov model of heat and mass flux is employed to analyze the heat and mass flow rates. The stretching velocities along x- and y-axes are, respectively, $U_w = ax$ and $V_w = by$. The z-axis is taken normal to the fluid flow.

The governing model of the flow consists of the following equations:

$$\frac{\partial u}{\partial x} + \frac{\partial v}{\partial y} + \frac{\partial w}{\partial z} = 0, \tag{1}$$

$$u\frac{\partial u}{\partial x} + v\frac{\partial u}{\partial y} + w\frac{\partial u}{\partial z} = v\frac{A}{\overline{C}}\frac{\partial^2 u}{\partial z^2} + v\frac{A}{2\overline{C}^3}\left(\frac{\partial u}{\partial z}\right)^2\frac{\partial^2 u}{\partial z^2} - \left(\frac{v}{K^*} + Fu\right)u, \tag{2}$$

$$u\frac{\partial v}{\partial x} + v\frac{\partial v}{\partial y} + w\frac{\partial v}{\partial z} = v\frac{A}{\overline{C}}\frac{\partial^2 v}{\partial z^2} + v\frac{A}{2\overline{C}^3}\left(\frac{\partial v}{\partial z}\right)^2\frac{\partial^2 v}{\partial z^2}, \tag{3}$$

$$\begin{aligned}
u\frac{\partial T}{\partial x} + v\frac{\partial T}{\partial y} &+ w\frac{\partial T}{\partial z} + \lambda_E\left(u\frac{\partial u}{\partial x}\frac{\partial T}{\partial x} + v\frac{\partial u}{\partial y}\frac{\partial T}{\partial x} + w\frac{\partial u}{\partial z}\frac{\partial T}{\partial x} + u\frac{\partial v}{\partial x}\frac{\partial T}{\partial y}\right. \\
&+ v\frac{\partial v}{\partial y}\frac{\partial T}{\partial y} + w\frac{\partial v}{\partial z}\frac{\partial T}{\partial y} + u\frac{\partial w}{\partial x}\frac{\partial T}{\partial z} + v\frac{\partial w}{\partial y}\frac{\partial T}{\partial z} + w\frac{\partial w}{\partial z}\frac{\partial T}{\partial z} + 2uv\frac{\partial^2 T}{\partial x\,\partial y} \\
&\left.+ 2vw\frac{\partial^2 T}{\partial y\,\partial z} + 2uw\frac{\partial^2 T}{\partial x\,\partial z} + u^2\frac{\partial^2 T}{\partial x^2} + v^2\frac{\partial^2 T}{\partial y^2} + w^2\frac{\partial^2 T}{\partial z^2}\right) = \alpha^*\frac{\partial^2 T}{\partial z^2},
\end{aligned} \tag{4}$$

$$\begin{aligned}
u\frac{\partial C}{\partial x} + v\frac{\partial C}{\partial y} &+ w\frac{\partial C}{\partial z} + \lambda_C\left(u\frac{\partial u}{\partial x}\frac{\partial C}{\partial x} + v\frac{\partial u}{\partial y}\frac{\partial C}{\partial x} + w\frac{\partial u}{\partial z}\frac{\partial C}{\partial x} + u\frac{\partial v}{\partial x}\frac{\partial C}{\partial y}\right. \\
&+ v\frac{\partial v}{\partial y}\frac{\partial C}{\partial y} + w\frac{\partial v}{\partial z}\frac{\partial C}{\partial y} + u\frac{\partial w}{\partial x}\frac{\partial C}{\partial z} + v\frac{\partial w}{\partial y}\frac{\partial C}{\partial z} + w\frac{\partial w}{\partial z}\frac{\partial C}{\partial z} + 2uv\frac{\partial^2 C}{\partial x\,\partial y} \\
&\left.+ 2vw\frac{\partial^2 C}{\partial y\,\partial z} + 2uw\frac{\partial^2 C}{\partial x\,\partial z} + u^2\frac{\partial^2 C}{\partial x^2} + v^2\frac{\partial^2 C}{\partial y^2} + w^2\frac{\partial^2 C}{\partial z^2}\right) = D\frac{\partial^2 C}{\partial z^2}.
\end{aligned} \tag{5}$$

The flow satisfies the following conditions:

$$\left\{\begin{array}{l} u = U_w = ax, v = V_w = by, w = 0, C = C_w, T = T_w \text{ at } z = 0, \\ v \longrightarrow 0, u \longrightarrow 0, C \longrightarrow C_\infty, T \longrightarrow T_\infty \text{ as } z \longrightarrow \infty. \end{array}\right\} \tag{6}$$

Here, u, v, and w are the velocity Cartesian components, $v = \mu/\rho_f$ is the kinematic viscosity, μ is the fluid dynamic viscosity, ρ_f is the fluid density, A and $\overline{C}$ are the material constants for the Prandtl liquid, λ_E is the relaxation time of heat flux, $F = c_b/x\sqrt{K^*}$ is the inertia coefficient, λ_C is the relaxation of mass flux, $\alpha^* = k/(\rho c)_f$ is the thermal diffusivity, k is the thermal conductivity, $(\rho c)_f$ is the heat capacity of working liquid, $(\rho c)_p$ is the effective heat capacity of nanoparticles, T is the temperature, C is the concentration, T_w is the surface temperature, C_w is the surface concentration, T_∞ is the ambient temperature, C_w is the ambient concentration, and D is the mass diffusion coefficient.

The similarity transformations are defined as

$$\left\{\begin{array}{l} u = ax\widetilde{f}'(\eta), v = ay\widetilde{g}'(\eta), w = -\sqrt{av}\left\{\widetilde{f}(\eta) + \widetilde{g}(\eta)\right\}, \\ \\ \theta(\eta) = \dfrac{T - T_\infty}{T_w - T_\infty}, \phi(\eta) = \dfrac{C - C_\infty}{C_w - C_\infty}, \eta = \sqrt{\dfrac{a}{v}}z. \end{array}\right\}. \tag{7}$$

Using these transformations, the continuity equation is satisfied identically, whereas equations (2)–(6) are transformed as
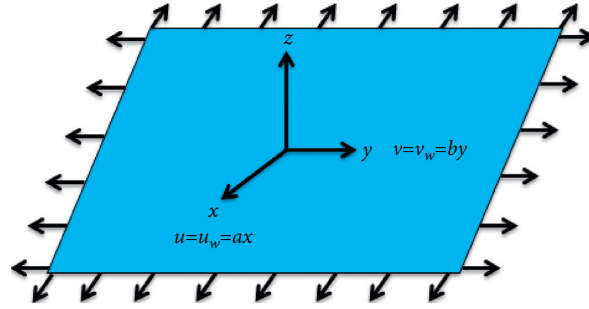
FIGURE 1: Configuration of the flow map.

$$\alpha_1 \widetilde{f}''' + \widetilde{g}\widetilde{f}'' + \widetilde{f}\widetilde{f}'' - \widetilde{f}'^2 + \alpha_2 \widetilde{f}'' \widetilde{f}''^2 - K\widetilde{f}' - Fr\widetilde{f}'^2 = 0, \tag{8}$$

$$\alpha_1 \widetilde{g}''' + \widetilde{f}\widetilde{g}'' + \widetilde{g}\widetilde{g}'' - \widetilde{g}'^2 + \alpha_2 \widetilde{g}'' \widetilde{g}''^2 = 0, \tag{9}$$

$$\widetilde{\theta}'' + \Pr\left[\widetilde{f}\widetilde{\theta}' + \widetilde{g}\widetilde{\theta}' - \gamma_e\left\{\widetilde{\theta}'\left(\widetilde{g}\widetilde{f}' + \widetilde{g}\widetilde{g}' + \widetilde{f}\widetilde{f}' + \widetilde{f}\widetilde{g}'\right) + \left(\widetilde{g}^2 + \widetilde{f}^2 + 2\widetilde{g}\widetilde{f}\right)\widetilde{\theta}''\right\}\right] = 0, \tag{10}$$

$$\widetilde{\phi}'' + Sc\left[\widetilde{f}\widetilde{\phi}' + \widetilde{g}\widetilde{\phi}' - \gamma_c\left\{\widetilde{\phi}'\left(\widetilde{g}\widetilde{f}' + \widetilde{g}\widetilde{g}' + \widetilde{f}\widetilde{f}' + \widetilde{f}\widetilde{g}'\right) + \left(\widetilde{g}^2 + \widetilde{f}^2 + 2\widetilde{g}\widetilde{f}\right)\widetilde{\phi}''\right\}\right] = 0, \tag{11}$$

$$\left\{\begin{array}{l}\widetilde{f}(0) = 0, \widetilde{f}'(0) = 1, \widetilde{f}'(\infty) \longrightarrow 0, \widetilde{g}(0) = 0, \widetilde{g}'(0) = \alpha, \\ \widetilde{g}'(\infty) \longrightarrow 0, \widetilde{\theta}(0) = 1, \widetilde{\theta}(\infty) \longrightarrow 0, \widetilde{\phi}(0) = 1, \widetilde{\phi}(\infty) \longrightarrow 0\end{array}\right\}, \tag{12}$$

where α, α_1, α_2, γ_c, γ_e, Pr, Sc, Fr, and K are respectively the ratio parameter, Prandtl fluid parameter, elastic parameter, concentration parameter, thermal relaxation parameter, Prandtl number, Schmidt number, inertia parameter, and porosity parameter. These are given by

$$\alpha = \frac{b}{a},$$

$$\alpha_1 = \frac{1}{\mu A\overline{C}},$$

$$\alpha_2 = \frac{bax}{2\overline{C}^2 v},$$

$$\gamma_e = a\lambda_E,$$

$$\gamma_c = a\lambda_C, \tag{13}$$

$$\Pr = \frac{v}{\alpha^*},$$

$$Sc = \frac{v}{D},$$

$$Fr = \frac{c_b}{\sqrt{K^*}},$$

$$K = \frac{v}{aK^*}.$$

The skin frication coefficients, heat transfer rate, and mass flow rate are defined as

$$\left\{\begin{array}{l}\sqrt{\mathrm{Re}_x}\, C_f = \alpha_1 \widetilde{f''}(0) + \alpha_2\left(\widetilde{f''}(0)\right)^3 \\[3mm] \sqrt{\mathrm{Re}_y}\, C_g = \alpha_1 \widetilde{g''}(0) + \alpha_2\left(\widetilde{g''}(0)\right)^3 \\[3mm] \dfrac{Nu_x}{\sqrt{\mathrm{Re}_x}} = -\widetilde{\theta}'(0) \\[3mm] \dfrac{Sh_x}{\sqrt{\mathrm{Re}_x}} = -\widetilde{\phi}'(0)\end{array}\right\}, \tag{14}$$

where $\mathrm{Re}_x = ax^2/v$ and $\mathrm{Re}_y = ay^2/v$ indicate the local Reynolds numbers. The present fluid reduces to the Newtonian fluid when $\alpha_1 = 1$ and $\alpha_2 = 0$.

3. Solution Methodology

In order to solve the nonlinear system of equations (8)–(11) subjected to the conditions in equation (12), we employ the homotopic scheme. The following steps are needed to execute the HAM procedure. The solution having the auxiliary constraint $\hbar$ adjusts and regulates the convergence of the analytical series solution.

The initial guesses are

$$\widetilde{f}_0(\eta) = 1 - e^{-\eta},$$
$$\widetilde{g}_0(\eta) = \alpha(1 - e^{-\eta}),$$
$$\widetilde{\theta}_0(\eta) = e^{-\eta}, \tag{15}$$
$$\widetilde{\phi}_0(\eta) = e^{-\eta}.$$

The linear operators $L_{\widetilde{f}}, L_{\widetilde{g}}, L_{\widetilde{\theta}}, L_{\widetilde{\phi}}$ are represented by

$$L_{\widetilde{f}}(\widetilde{f}) = \widetilde{f}''' - \widetilde{f}',$$
$$L_{\widetilde{g}}(\widetilde{g}) = \widetilde{g}''' - \widetilde{g}',$$
$$L_{\widetilde{\theta}}(\widetilde{\theta}) = \widetilde{\theta}'' - \widetilde{\theta}, \tag{16}$$
$$L_{\widetilde{\phi}}(\widetilde{\phi}) = \widetilde{\phi}'' - \widetilde{\phi},$$

with the following properties:

$$L_{\widetilde{f}}(\widetilde{c}_1 + \widetilde{c}_2 e^{-\eta} + \widetilde{c}_3 e^{\eta}) = 0,$$
$$L_{\widetilde{g}}(\widetilde{c}_4 + \widetilde{c}_5 e^{-\eta} + \widetilde{c}_6 e^{\eta}) = 0,$$
$$L_{\widetilde{\theta}}(\widetilde{c}_7 e^{\eta} + \widetilde{c}_8 e^{-\eta}) = 0, \tag{17}$$
$$L_{\widetilde{\phi}}(\widetilde{c}_9 e^{\eta} + \widetilde{c}_{10} e^{-\eta}) = 0,$$

where all $\widetilde{c}_i (i = 1 - 10)$ are numbers in the general solution.

The subsequent nonlinear operators $\widetilde{N}_{\widetilde{f}}, \widetilde{N}_{\widetilde{g}}, \widetilde{N}_{\widetilde{\theta}} \widetilde{N}_{\widetilde{\phi}}$ are given as

$$\widetilde{N}_{\widetilde{f}}[\widetilde{f}(\eta;\widetilde{p}), \widetilde{g}(\eta;\widetilde{p})] = \alpha_1 \frac{\partial^3 \widetilde{f}(\eta;\widetilde{p})}{\partial \eta^3} + g(\eta;\widetilde{p})\frac{\partial^2 \widetilde{f}(\eta;\widetilde{p})}{\partial \eta^2} + \widetilde{f}(\eta;\widetilde{p})\frac{\partial^2 \widetilde{f}(\eta;\widetilde{p})}{\partial \eta^2}$$

$$- \left(\frac{\partial \widetilde{f}(\eta;\widetilde{p})}{\partial \eta}\right)^2 + \alpha_2 \frac{\partial^3 \widetilde{f}(\eta;\widetilde{p})}{\partial \eta^3}\left(\frac{\partial^2 \widetilde{f}(\eta;\widetilde{p})}{\partial \eta^2}\right)^2 - K\frac{\partial \widetilde{f}(\eta;\widetilde{p})}{\partial \eta} - Fr\left(\frac{\partial \widetilde{f}(\eta;\widetilde{p})}{\partial \eta}\right)^2, \tag{18}$$

$$N_{\widetilde{g}}[\widetilde{f}(\eta;\widetilde{p}), \widetilde{g}(\eta;\widetilde{p})] = \alpha_1 \frac{\partial^3 \widetilde{g}(\eta;\widetilde{p})}{\partial \eta^3} + \widetilde{f}(\eta;p)\frac{\partial^2 \widetilde{g}(\eta;\widetilde{p})}{\partial \eta^2}$$

$$+ \widetilde{g}(\eta;\widetilde{p})\frac{\partial^2 \widetilde{g}(\eta;\widetilde{p})}{\partial \eta^2} - \left(\frac{\partial \widetilde{g}(\eta;\widetilde{p})}{\partial \eta}\right)^2 + \alpha_2 \frac{\partial^3 \widetilde{g}(\eta;\widetilde{p})}{\partial \eta^3}\left(\frac{\partial^2 \widetilde{g}((\eta;\widetilde{p})}{\partial \eta^2}\right)^2, \tag{19}$$

$$N_{\widetilde{\theta}}[\widetilde{f}(\eta;\widetilde{p}), \widetilde{g}(\eta;\widetilde{p}), \widetilde{\theta}(\eta;\widetilde{p})] = \frac{\partial^2 \widetilde{\theta}(\eta;\widetilde{p})}{\partial \eta^2} +$$

$$Pr\left[\begin{array}{c} \widetilde{f}(\eta;\widetilde{p})\dfrac{\partial \widetilde{\theta}(\eta;\widetilde{p})}{\partial \eta} + \widetilde{g}(\eta;\widetilde{p})\dfrac{\partial \widetilde{\theta}(\eta;\widetilde{p})}{\partial \eta} \\ -\gamma_e\left\{\dfrac{\partial \widetilde{\theta}(\eta;\widetilde{p})}{\partial \eta}\left(\begin{array}{c}\widetilde{g}(\eta;\widetilde{p})\dfrac{\partial \widetilde{f}(\eta;\widetilde{p})}{\partial \eta} + \widetilde{g}(\eta;\widetilde{p})\dfrac{\partial \widetilde{g}(\eta;\widetilde{p})}{\partial \eta} + \widetilde{f}(\eta;\widetilde{p})\dfrac{\partial \widetilde{f}(\eta;\widetilde{p})}{\partial \eta} + \\ \widetilde{f}(\eta;\widetilde{p})\dfrac{\partial \widetilde{g}(\eta;\widetilde{p})}{\partial \eta}\end{array}\right) + \\ \left((\widetilde{g}(\eta;\widetilde{p}))^2 + (\widetilde{f}(\eta;\widetilde{p}))^2 + 2\widetilde{g}(\eta;\widetilde{p})\widetilde{f}(\eta;\widetilde{p})\right)\dfrac{\partial^2 \widetilde{\theta}(\eta;\widetilde{p})}{\partial \eta^2}\end{array}\right\}\end{array}\right], \tag{20}$$

$$N_{\widetilde{\phi}}[\widetilde{f}(\eta;\widetilde{p}),\widetilde{g}(\eta;\widetilde{p}),\widetilde{\phi}(\eta;\widetilde{p})] = \frac{\partial^2\widetilde{\phi}(\eta;\widetilde{p})}{\partial\eta^2}+$$

$$Sc\left[\begin{array}{c}\widetilde{f}(\eta;\widetilde{p})\dfrac{\partial\widetilde{\phi}(\eta;\widetilde{p})}{\partial\eta}+\widetilde{g}(\eta;\widetilde{p})\dfrac{\partial\widetilde{\phi}(\eta;\widetilde{p})}{\partial\eta}\\[4mm] -\gamma_c\left\{\dfrac{\partial\widetilde{\phi}(\eta;\widetilde{p})}{\partial\eta}\left(\begin{array}{c}\widetilde{g}(\eta;\widetilde{p})\dfrac{\partial\widetilde{f}(\eta;\widetilde{p})}{\partial\eta}+\widetilde{g}(\eta;\widetilde{p})\dfrac{\partial\widetilde{g}(\eta;\widetilde{p})}{\partial\eta}+\widetilde{f}(\eta;\widetilde{p})\dfrac{\partial\widetilde{f}(\eta;\widetilde{p})}{\partial\eta}+\\[4mm]\widetilde{f}(\eta;\widetilde{p})\dfrac{\partial\widetilde{g}(\eta;\widetilde{p})}{\partial\eta}\end{array}\right)+\right.\\[6mm]\left.\left((\widetilde{g}(\eta;\widetilde{p}))^2+(\widetilde{f}(\eta;\widetilde{p}))^2+2\widetilde{g}(\eta;\widetilde{p})\widetilde{f}(\eta;\widetilde{p})\right)\dfrac{\partial^2\widetilde{\phi}(\eta;\widetilde{p})}{\partial\eta^2},\right\}\end{array}\right].$$

$$(21)$$

The basics of HAM have been explained in references [36]. The 0th-order problem from the system of equations (8)–(11) is

$$(1-\widetilde{p})L_{\widetilde{f}}\left[\widetilde{f}(\eta;\widetilde{p})-\widetilde{f}_0(\eta)\right]=\widetilde{p}\hbar_{\widetilde{f}}\widetilde{N}_{\widetilde{f}}[\widetilde{f}(\eta;\widetilde{p}),\widetilde{g}(\eta;\widetilde{p})],\tag{22}$$

$$(1-\widetilde{p}))L_{\widetilde{g}}\left[\widetilde{g}(\eta;\widetilde{p})-\widetilde{g}_0(\eta)\right]=\widetilde{p}\hbar_{\widetilde{g}}\widetilde{N}_{\widetilde{g}}[\widetilde{f}(\eta;\widetilde{p}),\widetilde{g}(\eta;\widetilde{p})],\tag{23}$$

$$(1-\widetilde{p})L_{\widetilde{\theta}}\left[\widetilde{\theta}(\eta;\widetilde{p})-\widetilde{\theta}_0(\eta)\right]=\widetilde{p}\hbar_{\widetilde{\theta}}\widetilde{N}_{\widetilde{\theta}}[\widetilde{f}(\eta;\widetilde{p}),\widetilde{g}(\eta;\widetilde{p}),\widetilde{\theta}(\eta;\widetilde{p})],\tag{24}$$

$$(1-\widetilde{p})L_{\widetilde{\phi}}\left[\widetilde{\phi}(\eta;\widetilde{p})-\widetilde{\phi}_0(\eta)\right]=\widetilde{p}\hbar_{\widetilde{\phi}}\widetilde{N}_{\widetilde{\phi}}[\widetilde{f}(\eta;\widetilde{p}),\widetilde{g}(\eta;\widetilde{p}),\widetilde{\phi}(\eta;\widetilde{p})].\tag{25}$$

The extreme values are

$$\widetilde{f}(\eta;\widetilde{p})|_{\eta=0}=0,\frac{\partial\widetilde{f}(\eta;\widetilde{p})}{\partial\eta}\bigg|_{\eta=0}=1,\frac{\partial\widetilde{f}(\eta;\widetilde{p})}{\partial\eta}\bigg|_{\eta\longrightarrow\infty}=0,$$

$$\widetilde{g}(\eta;\widetilde{p})|_{\eta=0}=0,\frac{\partial\widetilde{g}(\eta;\widetilde{p})}{\partial\eta}\bigg|_{\eta=0}=\alpha,\frac{\partial\widetilde{g}(\eta;\widetilde{p})}{\partial\eta}\bigg|_{\eta\longrightarrow\infty}=0,$$

$$\widetilde{\theta}(\eta;\widetilde{p})|_{\eta=0}=1,\widetilde{\theta}(\eta;\widetilde{p})\big|_{\eta\longrightarrow\infty}=0,\widetilde{\phi}(\eta;\widetilde{p})\big|_{\eta=0}$$

$$=1,\widetilde{\phi}(\eta;\widetilde{p})|_{\eta\longrightarrow\infty}=0,$$

$$(26)$$

where $\widetilde{p}\in[0,1]$ is the embedding parameter, and $\hbar_{\widetilde{f}},\hbar_{\widetilde{g}},\hbar_{\widetilde{p}},\hbar_{\widetilde{\phi}}$ are used to control the convergence of the obtained solution.

When $\widetilde{p}=0$ and $\widetilde{p}=1$, we have

$$\widetilde{f}(\eta;1)=\widetilde{f}(\eta),\widetilde{g}(\eta;1)=\widetilde{g}(\eta),\widetilde{\theta}(\eta;1)$$
$$=\widetilde{\theta}(\eta),\widetilde{\phi}(\eta;1)=\widetilde{\phi}(\eta).\tag{27}$$

The Taylor's series expansions of $\widetilde{f}(\eta;\widetilde{p}),\widetilde{g}(\eta;\widetilde{p}),\widetilde{\theta}(\eta;\widetilde{p}),\widetilde{\phi}(\eta;\widetilde{p})$ about $\widetilde{p}=0$ are given by

$$\widetilde{f}(\eta;\widetilde{p})=\widetilde{f}_0(\eta)+\sum_{m=1}^{\infty}\widetilde{f}_m(\eta)\widetilde{p}^m,$$

$$\widetilde{g}(\eta;\widetilde{p})=\widetilde{g}_0(\eta)+\sum_{m=1}^{\infty}\widetilde{g}_m(\eta)\widetilde{p}^m,$$

$$\widetilde{\theta}(\eta;\widetilde{p})=\widetilde{\theta}_0(\eta)+\sum_{m=1}^{\infty}\widetilde{\theta}_m(\eta)\widetilde{p}^m,\tag{28}$$

$$\widetilde{\phi}((\eta;\widetilde{p})=\widetilde{\phi}_0(\eta)+\sum_{m=1}^{\infty}\widetilde{\phi}_m(\eta)\widetilde{p}^m,$$

whereas

$$\widetilde{f}_m(\eta)=\frac{1}{m!}\frac{\partial\widetilde{f}(\eta;\widetilde{p})}{\partial\eta}\bigg|_{\widetilde{p}=0},$$

$$\widetilde{g}_m(\eta)=\frac{1}{m!}\frac{\partial\widetilde{g}(\eta;\widetilde{p})}{\partial\eta}\bigg|_{\widetilde{p}=0},$$

$$\widetilde{\theta}_m(\eta)=\frac{1}{m!}\frac{\partial\theta(\eta;\widetilde{p})}{\partial\eta}\bigg|_{\widetilde{p}=0},\tag{29}$$

$$\widetilde{\phi}_m(\eta)=\frac{1}{m!}\frac{\partial\phi(\eta;\widetilde{p})}{\partial\eta}\bigg|_{\widetilde{p}=0}.$$

The secondary constraints $\hbar_{\widetilde{f}}, \hbar_{\widetilde{g}}, \hbar_{\widetilde{\theta}}, \hbar_{\widetilde{\phi}}$ are chosen in such a way that series (27) converges at $\widetilde{p} = 1$. Substituting $\widetilde{p} = 1$ in equation (27), we get

$$\widetilde{f}(\eta) = \widetilde{f}_0(\eta) + \sum_{m=1}^{\infty} \widetilde{f}_m(\eta),$$

$$\widetilde{g}(\eta) = \widetilde{g}_0(\eta) + \sum_{m=1}^{\infty} \widetilde{g}_m(\eta),$$

$$\widetilde{\theta}(\eta) = \widetilde{\theta}_0(\eta) + \sum_{m=1}^{\infty} \widetilde{\theta}_m(\eta),$$

$$\widetilde{\phi}(\eta) = \widetilde{\phi}_0(\eta) + \sum_{m=1}^{\infty} \widetilde{\phi}_m(\eta).$$

(30)

The $m^{th} - order$ problem satisfies the following relations:

$$L_{\widetilde{f}}\left[\widetilde{f}_m(\eta) - \chi_m \widetilde{f}_{m-1}(\eta)\right] = \hbar_{\widetilde{f}} \widetilde{R}_m^{f}(\eta),$$

$$L_{\widetilde{g}}\left[\widetilde{g}_m(\eta) - \chi_m \widetilde{g}_{m-1}(\eta)\right] = \hbar_{\widetilde{g}} \widetilde{R}_m^{g}(\eta),$$

$$L_{\widetilde{\theta}}\left[\widetilde{\theta}_m(\eta) - \chi_m \widetilde{\theta}_{m-1}(\eta)\right] = \hbar_{\widetilde{\theta}} \widetilde{R}_m^{\theta}(\eta),$$

$$L_{\widetilde{\phi}}\left[\widetilde{\phi}_m(\eta) - \chi_m \widetilde{\phi}_{m-1}(\eta)\right] = \hbar_{\widetilde{\phi}} \widetilde{R}_m^{\phi}(\eta).$$

(31)

The corresponding boundary conditions are

$$\widetilde{f}_m(0) = \widetilde{f}_m'(0) = \widetilde{g}_m(0) = \widetilde{g}_m'(0) = \widetilde{\theta}_m(0) = \widetilde{\phi}_m(0) = 0,$$

$$\widetilde{f}_m'(\infty) = \widetilde{g}_m'(\infty) = \widetilde{\theta}_m'(\infty) = \widetilde{\phi}_m'(\infty) = 0.$$

(32)

The different symbols in equation (30) represent the following expressions:

$$\widetilde{R}_m^{f}(\eta) = \alpha_1 \widetilde{f}_{m-1}'' + \sum_{k=0}^{m-1} \widetilde{g}_{m-1-k}'' \widetilde{f}_k'' + \sum_{k=0}^{m-1} \widetilde{f}_{m-1-k} \widetilde{f}_k'' - \sum_{k=0}^{m-1} \widetilde{f}_{m-1-k}' \widetilde{f}_k' + \alpha_2 \sum_{k=0}^{m-1} \widetilde{f}_{m-1-k}'' \sum_{l=0}^{k} \widetilde{f}_{k-1}'' \widetilde{f}_l'' - K\widetilde{f}_{m-1}' - Fr \sum_{k=0}^{m-1} \widetilde{f}_{m-1-k}' \widetilde{f}_k'',$$

(33)

$$\widetilde{R}_m^{g}(\eta) = \alpha_1 \widetilde{g}_{m-1}'' + \sum_{k=0}^{m-1} \widetilde{f}_{m-1-k} \widetilde{g}_k'' + \sum_{k=0}^{m-1} \widetilde{g}_{m-1-k} \widetilde{g}_k'' - \sum_{k=0}^{m-1} \widetilde{g}_{m-1-k}' \widetilde{g}_k' + \alpha_2 \sum_{k=0}^{m-1} \widetilde{g}_{m-1-k}'' \sum_{l=0}^{k} \widetilde{g}_{k-l}'' \widetilde{g}_l'',$$

(34)

$$\widetilde{R}_m^{\theta}(\eta) = \widetilde{\theta}_{m-1}''$$

$$+ \Pr \left[\begin{array}{c} \sum_{k=0}^{m-1} \widetilde{f}_{m-1-k} \theta_k' + \sum_{k=0}^{m-1} \widetilde{g}_{m-1-k} \theta_k' - \\ \gamma_e \left\{ \begin{array}{c} \sum_{k=0}^{m-1} \widetilde{f}_{m-1-k}' \sum_{l=0}^{k} \widetilde{g}_{k-l} \widetilde{\theta}_l' + \sum_{k=0}^{m-1} \widetilde{g}_{m-1-k} \sum_{l=0}^{k} \widetilde{g}_{k-l}' \widetilde{\theta}_l' + \sum_{k=0}^{m-1} \widetilde{f}_{m-1-k} \sum_{l=0}^{k} \widetilde{f}_{k-l}' \widetilde{\theta}_l' + \sum_{k=0}^{m-1} \widetilde{f}_{m-1-k} \sum_{l=0}^{k} \widetilde{g}_{k-l}' \widetilde{\theta}_l' + \\ \sum_{k=0}^{m-1} \widetilde{g}_{m-1-k} \sum_{k=0}^{m-1} \widetilde{g}_{m-1-k} \widetilde{\theta}_l'' + \sum_{k=0}^{m-1} \widetilde{f}_{m-1-k} \sum_{k=0}^{m-1} \widetilde{f}_{m-1-k} \widetilde{\theta}_l'' + 2 \sum_{k=0}^{m-1} \widetilde{f}_{m-1-k} \sum_{k=0}^{m-1} \widetilde{g}_{m-1-k} \widetilde{\theta}_l'' \end{array} \right\} \end{array} \right],$$

(35)

$$\widetilde{R}_m^{\phi}(\eta) = \widetilde{\phi}_{m-1}'' + Sc \left[\begin{array}{c} \sum_{k=0}^{m-1} \widetilde{f}_{m-1-k} \widetilde{\phi}_k' + \sum_{k=0}^{m-1} \widetilde{g}_{m-1-k} \widetilde{\phi}_k' - \\ \gamma_c \left\{ \begin{array}{c} \sum_{k=0}^{m-1} \widetilde{f}_{m-1-k}' \sum_{l=0}^{k} \widetilde{g}_{k-l} \widetilde{\phi}_l' + \sum_{k=0}^{m-1} \widetilde{g}_{m-1-k} \sum_{l=0}^{k} \widetilde{g}_{k-l}' \widetilde{\phi}_l' + \sum_{k=0}^{m-1} \widetilde{f}_{m-1-k} \sum_{l=0}^{k} \widetilde{f}_{k-l}' \widetilde{\phi}_l' + \sum_{k=0}^{m-1} \widetilde{f}_{m-1-k} \sum_{l=0}^{k} \widetilde{g}_{k-l}' \widetilde{\phi}_l' + \\ \sum_{k=0}^{m-1} \widetilde{g}_{m-1-k} \sum_{k=0}^{m-1} \widetilde{g}_{m-1-k} \widetilde{\phi}_l'' + \sum_{k=0}^{m-1} \widetilde{f}_{m-1-k} \sum_{k=0}^{m-1} \widetilde{f}_{m-1-k} \widetilde{\phi}_l'' + 2 \sum_{k=0}^{m-1} \widetilde{f}_{m-1-k} \sum_{k=0}^{m-1} \widetilde{g}_{m-1-k} \widetilde{\phi}_l'' \end{array} \right\} \end{array} \right],$$

(36)

with

$$\chi_m = \begin{cases} 0, & \text{if } \widetilde{p} \le 1, \\ 1, & \text{if } \widetilde{p} > 1. \end{cases}$$

(37)

4. Convergence Analysis

The right selection of auxiliary constraints $\hbar_f, \hbar_f, \hbar_\theta,$ and $\hbar_\phi$ well affects the convergence of a series solution of a nonlinear governing problem by homotopic technique. The
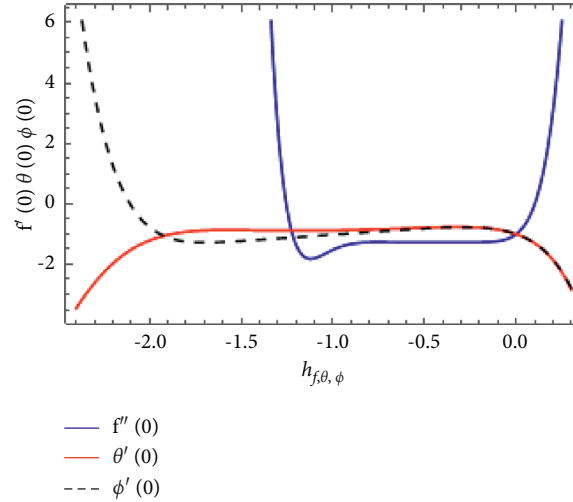
FIGURE 2: $\hbar-$ curves plot of the velocity, energy, and concentration profiles.

precise choice of these parameters plays a significant role in regulating the convergence zone. In this regard, we computed and sketched the velocity, temperature, and concentration plots in Figure 2. The interval of convergence is determined by the flat part of these plots. Tables 1 and 2 show the ranges of the permissible auxiliary parameter values and fruitful convergence. It is found that as the order of approximation upsurges, the average squared residual error diminishes, as shown in Figure 3. The comparison of the HAM solution with the shooting technique (RK-4) has been made to confirm the effectiveness of the implemented method. Results are shown graphically in Figures 3–6 and tabulated in Tables 3–6.

5. Results Analysis

This part is devoted to understand the physical consequences through the graphical display of the state variables of the investigated fluid flow. The system of nonlinear equations (8)–(11) with the extreme conditions in equation (12) are tackled via the famous analytical method of HAM. The impact on velocity, energy, and concentration profiles is explored graphically with the variation of various dimensionless parameters in Figures 2–10. The computational upshots for the drag force, heat, and mass flow rates are tabularized respectively in Tables 7–9. Table 7 represents the variation in the drag force coefficient with varying values of α_1, α_2, K, and Fr. It has been perceived that the drag force diminishes with the increasing α_1, α_2 values, while enhances with the augmenting K, Fr values. Table 8 displays the heat transfer features through variation of Nusselt number with varying Pr and γ_e. It is noticed that Joule heating increases with higher Prandtl number values and drops with the increasing thermal relaxation parameter. Table 9 displays the impact of varying strength of Sc and γ_c on the mass flow rate. The tale shows that the mass flow rate enhances with the increasing Schmidt number values and drops with the augmenting inertia parameter strength.

TABLE 1: The permissible ranges for the convergent solution.

Approximate solutions	Auxiliary parameters	Convergent intervals
$f(\eta)$	$\hbar_f$	$-0.7 \leq \hbar_f \leq -0.1$
$\theta(\eta)$	$\hbar_\theta$	$-1.6 \leq \hbar_\theta \leq -0.2$
$\phi(\eta)$	$\hbar_\phi$	$-0.5 \leq \hbar_\phi \leq -0.1$

Figures 8(a)–8(c) demonstrate the impact of Prandtl fluid parameter (α_1) variation over fluid velocity, thermal field, and concentration field, respectively. One can perceive that $f'(\eta)$ is the growing function of α_1. Thus, the fluid velocity and associated boundary layer thickness enhance with the rise in Prandtl fluid parameter. Here, the thermal field and concentration profile drop with the increasing α_1, and therefore, the boundary layer thickness diminishes in both cases. Figures 9(a)–9(c) depict the effect of elastic parameter (α_2) variation on the flow field, temperature distribution, and concentration, respectively. Figure 9(a) shows that the thickness of the momentum boundary layer boosts with the larger elastic parameter strength. The boosting is more prominent in the intermediate region. The increasing elastic parameter diminishes the heat conduction and escalates the heat convection. In consequence, the thermal field $\theta(\eta)$ curves and boundary layer thickness dwindle with the enhancing α_2 as displayed by Figure 9(b). The concentration field diminishes with the rising α_2 as displayed by Figure 9(c). Figure 10(a) illustrates the variation in the thermal field $(\theta(\eta))$ with the different values of thermal relaxation parameter (γ_e). This graph reveals that the temperature field decreases with the higher relaxation parameter strength. In fact, the working fluid dissipates extra heat with the augmenting thermal relaxation parameter. In consequence, the fluid temperature diminishes. Figure 10(b) delineates the impact of γ_c on the concentration profile $\phi(\eta)$. We see that higher estimation of γ_c retards the concentration and the related boundary layer thickness mitigates. In consequence, $\phi(\eta)$ reduces. Figures 11(a) and 11(b) present the outcome

TABLE 2: Series solution convergence analysis subjected to distinct order approximations.

M	$f(\eta)$	$g(\eta)$	$\theta(\eta)$	$\phi(\eta)$
4	1.43051×10^{-6}	0.0000213906	0.0000826203	0.0000276808
8	1.82262×10^{-9}	1.54095×10^{-7}	1.02815×10^{-6}	1.32032×10^{-7}
12	1.03571×10^{-11}	2.29034×10^{-9}	1.34154×10^{-8}	4.87951×10^{-10}
16	1.12675×10^{-13}	5.49984×10^{-11}	1.72623×10^{-10}	1.10127×10^{-12}
20	2.14918×10^{-15}	1.19988×10^{-12}	2.20574×10^{-12}	1.13712×10^{-15}
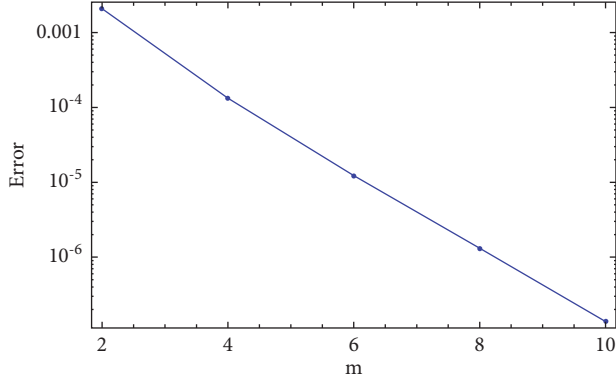
FIGURE 3: Squared residual via order of approximation.
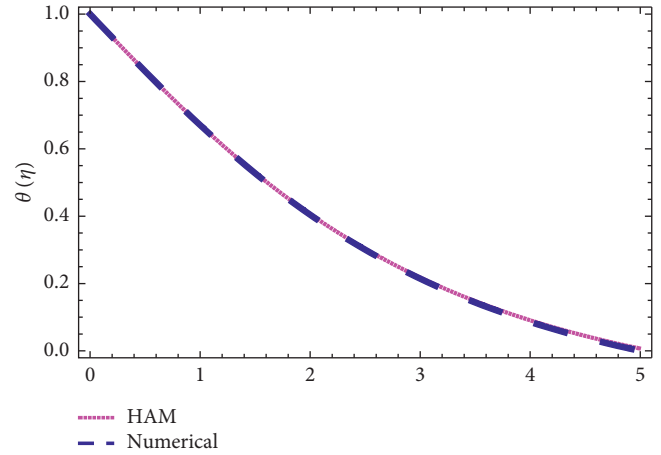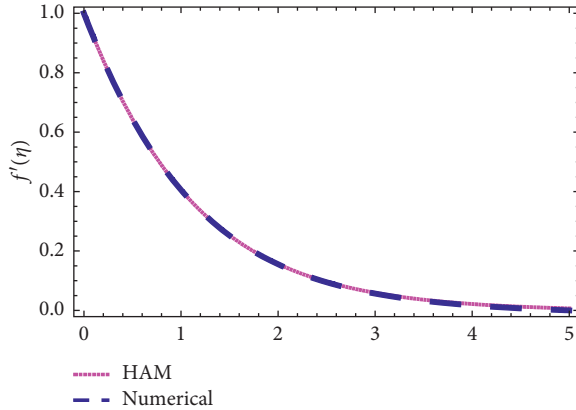
FIGURE 4: Comparison of the two solutions for $f'(\eta)$.

FIGURE 5: Comparison of the two solutions for $g(\eta)$.
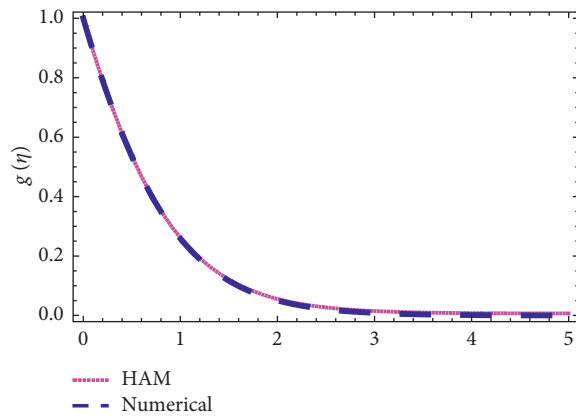
FIGURE 6: Comparison of the two solutions for $\theta(\eta)$.

TABLE 3: Comparison of the two solutions for $f'(\eta)$.

η	HAM solution	Numerical solution	Absolute error
0.0	1.000000	1.000000	0.000000
0.5	0.917840	0.917839	1.1×10^{-6}
1.0	0.841372	0.841369	2.7×10^{-6}
1.5	0.770370	0.770365	5.1×10^{-6}
2.0	0.704599	0.704590	8.6×10^{-6}
2.5	0.643808	0.643793	0.000014
3.0	0.587740	0.587717	0.000022
3.5	0.536131	0.536096	0.000034
4.0	0.488662	0.488662	0.000051
4.5	0.445145	0.445145	0.000073
5.0	0.405279	0.405279	0.000102

of porosity parameter (K) and inertia parameter (Fr) on the stream flow profiles. As anticipated, the velocity of material particles diminishes with the larger porosity and inertia parameters. Figure 12(a) shows the impact of variation of Prandtl number on the thermal field distribution. Clearly, the thermal field decreases with the higher strength of Pr. An upsurge in the Prandtl number declines the thermal diffusion in the fluid layers. In consequence, a thinner thermal boundary layer forms and the temperature field diminishes. Figure 12(b) portrays the Schmidt number (Sc) effect on the concentration profile $\phi(\eta)$. As we know that the Schmidt number and mass diffusion are related inversely with each other, hence an upsurge in Sc results in a decay in the concentration field as displayed in the figure.

TABLE 4: Comparison of the two solutions for $g(\eta)$.

η	HAM solution	Numerical solution	Absolute error
0.0	1.000000	1.000000	4.4×10^{-6}
0.5	0.891008	0.890713	0.000295
1.0	0.790149	0.789552	0.000597
1.5	0.697491	0.696584	0.000907
2.0	0.612988	0.611765	0.001223
2.5	0.536478	0.534936	0.001542
3.0	0.467693	0.465830	0.001863
3.5	0.406272	0.404089	0.002184
4.0	0.351778	0.349278	0.002500
4.5	0.303719	0.300908	0.002810
5.0	0.261568	0.258456	0.003112

TABLE 5: Comparison of the two solutions for $\theta(\eta)$.

η	HAM solution	Numerical solution	Absolute error
0.0	1.000000	1.000000	2.2×10^{-16}
0.5	0.965778	0.965706	0.000072
1.0	0.931640	0.931496	0.000144
1.5	0.931640	0.897453	0.000217
2.0	0.897670	0.863660	0.000291
2.5	0.863951	0.830198	0.000366
3.0	0.830564	0.797143	0.000443
3.5	0.797586	0.764564	0.000523
4.0	0.765086	0.732527	0.000604
4.5	0.701776	0.701088	0.000688
5.0	0.671072	0.670297	0.00755

TABLE 6: Comparison of the two solutions for $\phi(\eta)$.

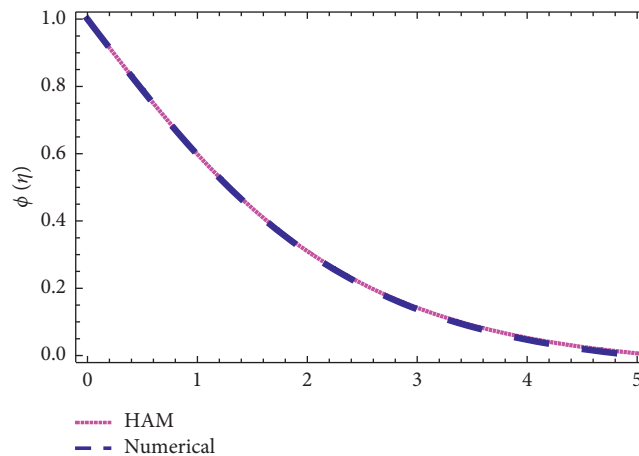| η	HAM solution	Numerical solution	Absolute error
0.0	1.000000	1.000000	0.000000
0.5	0.957396	0.957229	0.000168
1.0	0.914948	0.914673	0.000335
1.5	0.872812	0.872311	0.000501
2.0	0.83114	0.830477	0.000666
2.5	0.790091	0.789261	0.000830
3.0	0.749795	0.748803	0.000991
3.5	0.710383	0.709232	0.001151
4.0	0.671372	0.670664	0.001308
4.5	0.634660	0.633197	0.001462
5.0	0.538531	0.596917	0.001614

FIGURE 7: Comparison of the two solutions for $\phi(\eta)$.
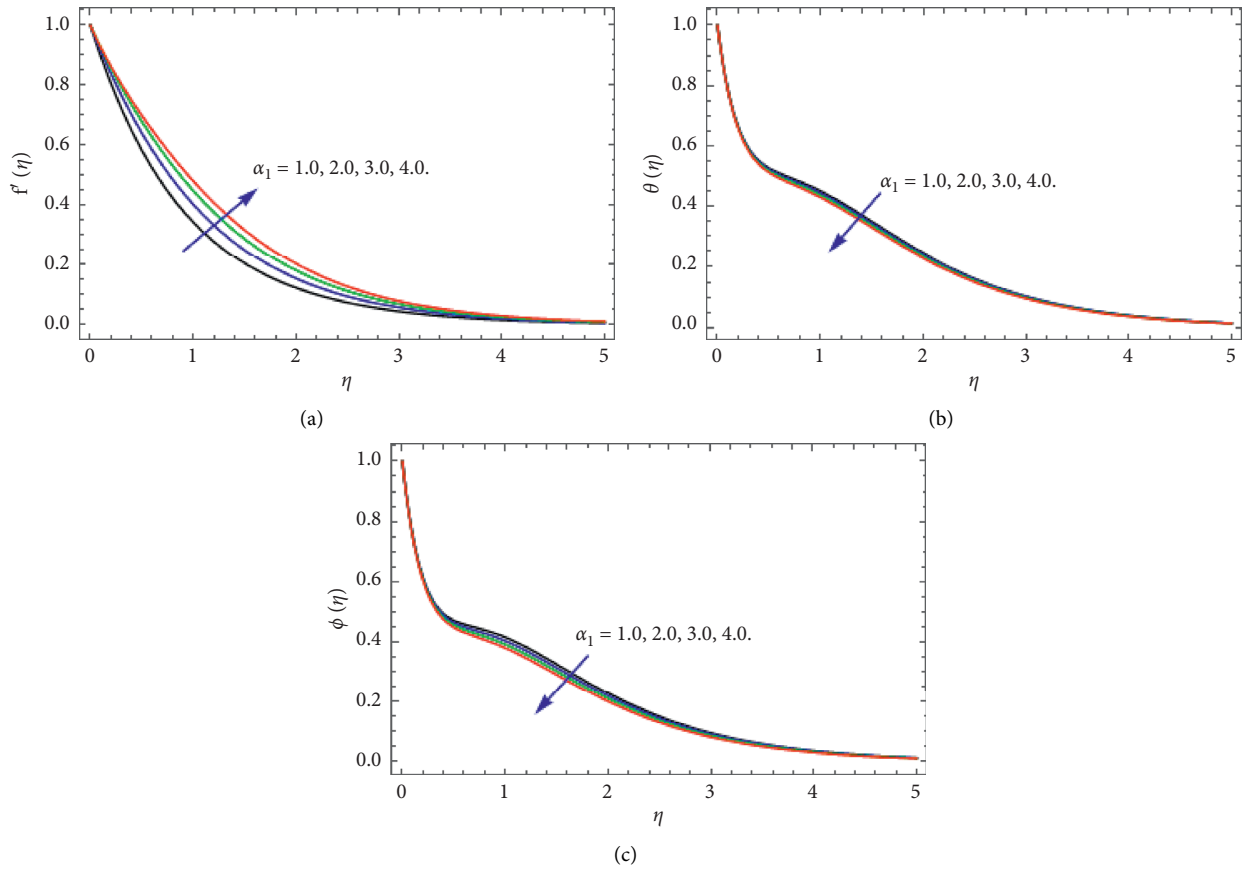
(a)

(b)

(c)

FIGURE 8: Effect of Prandtl fluid parameter on $f'(\eta)$, $\theta(\eta)$, $\phi(\eta)$. (a) Velocity profile. (b) Temperature field. (c) Concentration profile.
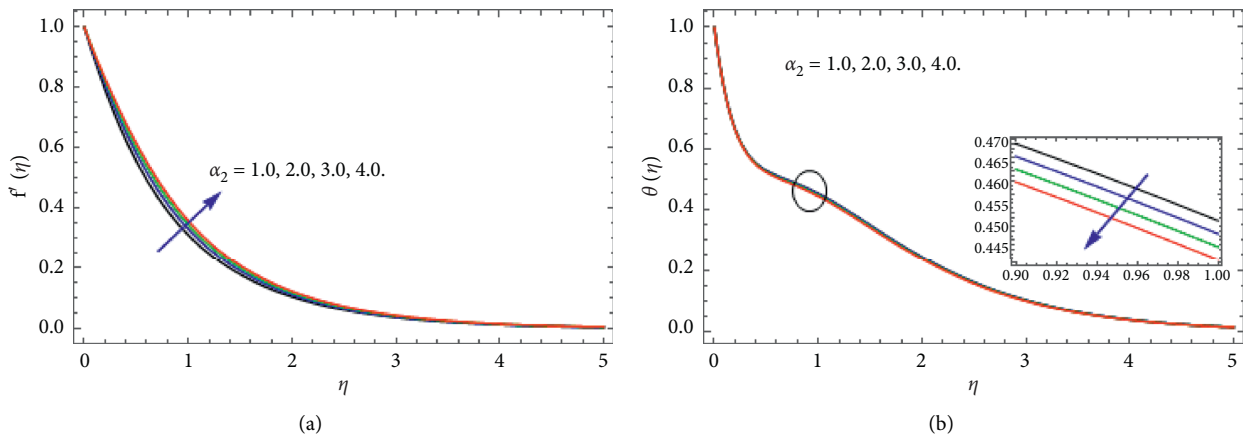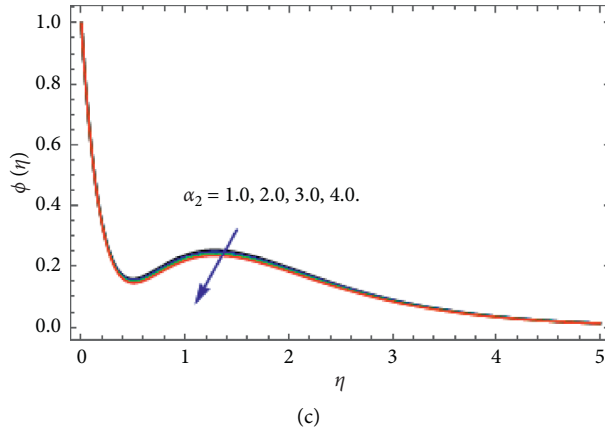

(a)

(b)

FIGURE 9: Continued.

(c)

FIGURE 9: Effect of elastic parameter on $f\prime(\eta)$, $\theta(\eta)$, $\phi(\eta)$. (a) Velocity profile. (b) Temperature field. (c) Concentration profile.
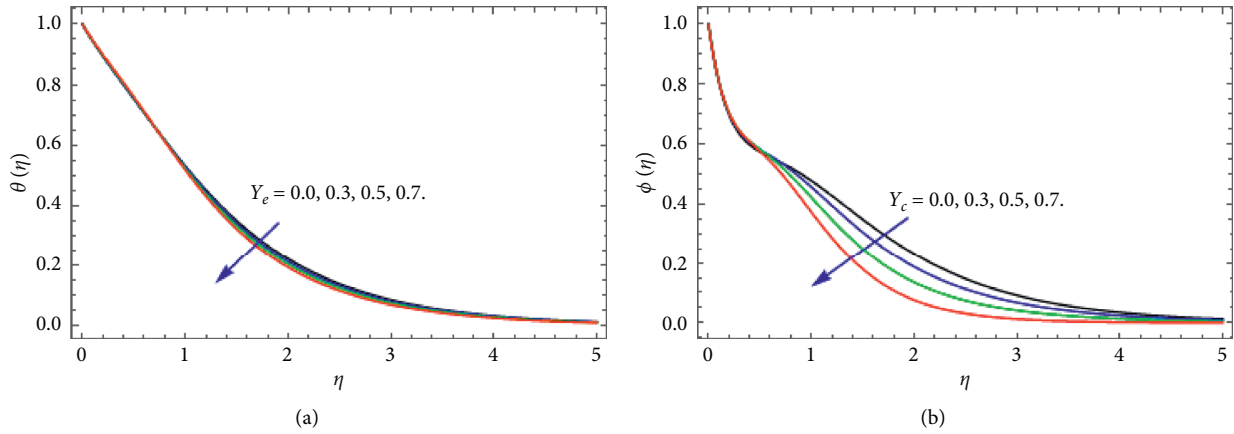

(a)

(b)

FIGURE 10: Effect of thermal relaxation parameter and concentration parameter on $\theta(\eta)$, $\phi(\eta)$. (a) Temperature field. (b) Concentration profile.

TABLE 7: Impact of different parameters on drag force.

$\alpha 1$	$\alpha 2$	K	Fr	$\sqrt{Re_x}C_f$
0.1	0.5	0.5	0.5	−0.273061
0.2				−0.267862
0.3				−0.26281
	0.5			−0.273061
	0.6			−0.26965
	0.7			−0.266325
		0.5		−0.273061
		0.6		−0.277752
		0.7		−0.282494
			0.5	
			0.6	−0.276538
			0.7	−0.280041

TABLE 8: Impact of Pr and γ_e on the Nusselt number.

Pr	γ_e	$Nu_x/\sqrt{Re_x}$
0.4	0.1	0.830990
0.5		0.868434
0.6		0.894973

Pr	γ_e	$Nu_x/\sqrt{Re_x}$
0.4	0.1	0.830990
	0.2	0.829404
	0.3	0.827812

TABLE 9: Impact of Sc and γ_c on the Sherwood number.

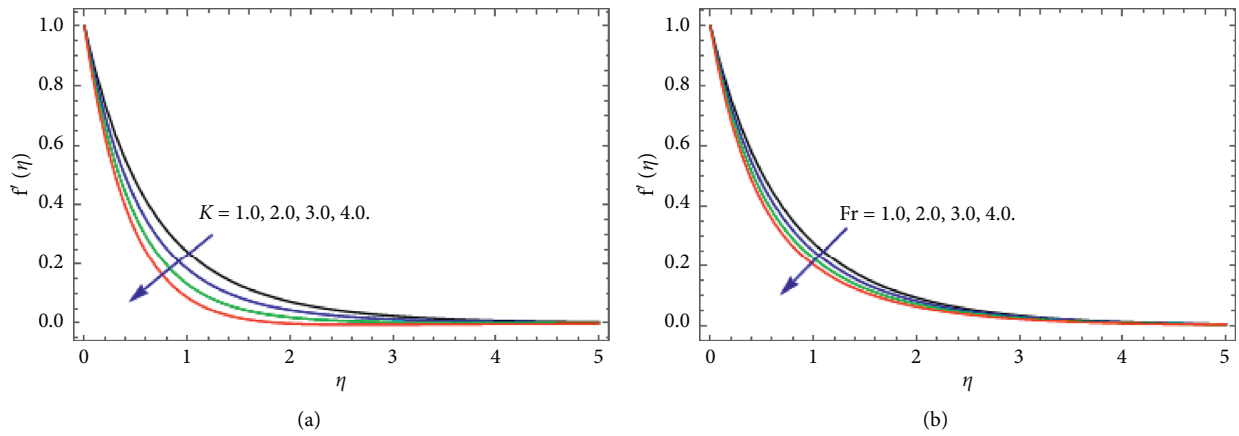| Sc	γ_c	$Sh_x/\sqrt{Re_x}$
0.2	0.1	0.682041
0.3		0.774562
0.4		0.830982
0.2	0.1	0.682041
	0.3	0.679379
	0.5	0.673995

FIGURE 11: The effect of the porosity parameter and inertia parameter on $f'(\eta)$. (a) Demonstration of velocity profile. (b) Velocity profile.
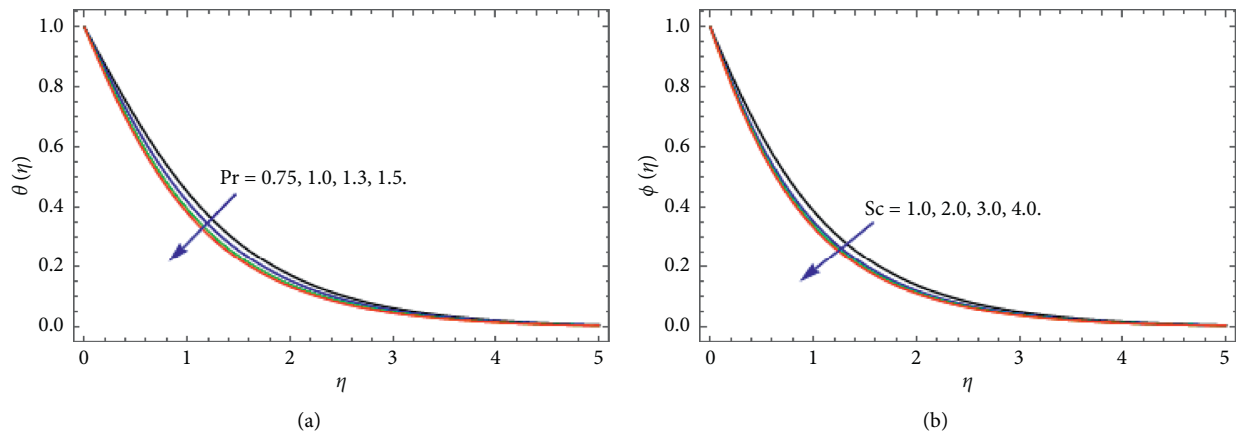

FIGURE 12: Effect of Prandtl and Schmidt numbers on $\theta(\eta)$, $\phi(\eta)$. (a) Temperature field. (b) Concentration profile.

6. Conclusions

This section concludes the findings of the undertaken research. In the current mathematical framework, the 3D Darcy–Forchheimer flow of Prandtl fluid motion over a nonlinear permeable surface with heat conduction and mass diffusion is considered. The Prandtl motion is modeled through coupled nonlinear PDEs. The system of PDEs is converted to a simplified set of coupled nonlinear ODEs using suitable similarity relations. HAM is applied to solve the reduced system of equations. The convergent analysis of the applied procedure shows that the solution is convergent

over a wide range. The comparison of HAM with the shooting technique through graphs and tables displays tremendous agreement. This research work has a wide range of applications in industrial and technological fields. The key points of the current work are outlined as follows:

> With the increase in Prandtl fluid parameter, the momentum boundary layer enhances, while the thermal and concentration boundary layers diminish
>
> The momentum boundary layer upsurges for larger elastic parameters, whereas both temperature and concentration fields dwindle
>
> The rising thermal relaxation and concentration parameters depict similar reducing behavior for the thermal and concentration fields
>
> The augmenting Schmidt number causes drop in the fluid concentration
>
> The drag force coefficient decreases with the enhancing Prandtl fluid t and elastic parameters

Data Availability

The data used to support the findings of this study are available from the corresponding author upon request.

Conflicts of Interest

The authors declare no conflicts of interest regarding the study in this paper.

Authors' Contributions

All authors have equally contributed in this paper.

References

[1] P. J. Carreau, "Rheological equations from molecular network theories," *Transactions of the Society of Rheology*, vol. 16, no. 1, pp. 99–127, 1972.

[2] P. J. Carreau, D. D. Kee, and M. Daroux, "An analysis of the viscous behaviour of polymeric solutions," *Canadian Journal of Chemical Engineering*, vol. 57, no. 2, pp. 135–140, 1979.

[3] N. S. Akbar, Z. H. Khan, and R. U. Haq, "Dual solutions in MHD stagnation-point flow of Prandtl fluid impinging on shrinking sheet," *Applied Mathematics and Mechanics*, vol. 35, no. 7, pp. 813–820, 2014.

[4] S. Bilal, "Effect logs of double diffusion on MHD Prandtl nano fluid adjacent to stretching surface by way of numerical approach," *Results in Physics*, vol. 7, pp. 470–479, 2017.

[5] S. Nadeem, H. Sadaf, and N. S. Akbar, "Analysis of peristaltic flow of Prandtl fluid model in an endoscope," *J Power Tech*, vol. 94, pp. 1–11, 2014.

[6] I. Khan, M. Y. Malik, A. Hussain, and T. Salahuddin, "Effect of homogenous-heterogeneous reactions on MHD Prandtl fluid flow over a stretching sheet," *Results in Physics*, vol. 7, pp. 4226–4231, 2017.

[7] C. H. Amanulla, S. Saleem, A. Wakif, and M. M. AlQarni, "MHD Prandtl fluid flow past an isothermal permeable sphere with slip effects," *Case Studies in Thermal Engineering*, vol. 14, Article ID 100447, 2019.

[8] S. Mukhopadhyay, "Slip effects on MHD boundary layer flow over an exponentially stretching sheet with suction/blowing and thermal radiation," *Ain Shams Engineering Journal*, vol. 4, no. 3, pp. 485–491, 2013.

[9] F. Ali and A. Zaib, "Unsteady flow of an Eyring-Powell nanofluid near stagnation point past a convectively heated stretching sheet," *Arab Journal of Basic and Applied Sciences*, vol. 26, no. 1, pp. 215–224, 2019.

[10] N. S. Akbar, "Blood flow analysis of Prandtl fluid model in tapered stenosed arteries," *Ain Shams Engineering Journal*, vol. 5, no. 4, pp. 1267–1275, 2014.

[11] S. Nadeem, S. Ijaz, and N. S. Akbar, "Nanoparticle analysis for blood flow of Prandtl fluid model with stenosis," *International Nano Letters*, vol. 3, no. 1, p. 35, 2013.

[12] T. Hayat, H. Zahir, A. Tanveer, and A. Alsaedi, "Influences of Hall current and chemical reaction in mixed convective peristaltic flow of Prandtl fluid," *Journal of Magnetism and Magnetic Materials*, vol. 407, pp. 321–327, 2016.

[13] Z. Khan, H. U. Rasheed, T. A. Alkanhal, M. Ullah, I. Khan, and I. Tlili, "Effect of magnetic field and heat source on Upper-convected-maxwell fluid in a porous channel," *Open Physics*, vol. 16, no. 1, pp. 917–928, 2018.

[14] Z. Khan, N. Tairan, W. K. Mashwani, H. U. Rasheed, H. Shah, and W. Khan, "MHD and slip effect on two-immiscible third grade fluid on thin film flow over a vertical moving belt," *Open Physics*, vol. 17, no. 1, pp. 575–586, 2019.

[15] H. U. Rasheed, Z. Khan, S. Islam et al., "Investigation of two-dimensional viscoelastic fluid with nonuniform heat generation over permeable stretching sheet with slip condition," *Complexity*, vol. 2019, Article ID 3121896, 8 pages, 2019.

[16] Z. Khan, H. U. Rasheed, Q. Shah, T. Abbas, and M. Ullah, "Numerical simulation of double-layer optical fiber coating using Oldroyd 8-constant fluid as a coating material," *Optical Engineering*, vol. 57, no. 7, Article ID 076104, 2018.

[17] Z. Khan, H. U. Rasheed, S. Noor et al., "Analytical solution of UCM viscoelastic liquid with slip condition and heat flux over stretching sheet: the galerkin approach," *Mathematical Problems in Engineering*, vol. 2020, Article ID 7563693, 7 pages, 2020.

[18] H. U. R. Rasheed, S. Islam, Z. Khan, S. O. Alharbi, H. Alotaibi, and I. Khan, "Impact of nanofluid flow over an elongated moving surface with a uniform hydromagnetic field and nonlinear heat reservoir," *Complexity*, vol. 2021, Article ID 9951162, 9 pages, 2021.

[19] Z. Khan, H. U. Rasheed, M. Ullah et al., "Shooting method analysis in wire coating withdrawing from a bath of Oldroyd 8-constant fluid with temperature dependent viscosity," *Open Physics*, vol. 16, no. 1, pp. 956–966, 2018.

[20] S. Z. Abbas, W. A. Khan, S. Kadry, M. I. Khan, M. Waqas, and M. I. Khan, "Entropy optimized Darcy-Forchheimer nanofluid (silicon dioxide, molybdenum disulfide) subject to temperature dependent viscosity," *Computer Methods and Programs in Biomedicine*, vol. 190, Article ID 105363, 2020.

[21] P. Sreedevi and P. S. Reddy, "Combined influence of Brownian motion and thermophoresis on Maxwell three-dimensional nanofluid flow over stretching sheet with chemical reaction and thermal radiation," *Journal of Porous Media*, vol. 23, no. 4, 2020.

[22] S. Islam, H. Ur Rasheed, K. S. Nisar, N. A. Alshehri, and M. Zakarya, "Numerical simulation of heat mass transfer effects on MHD flow of Williamson nanofluid by a stretching surface with thermal conductivity and variable thickness," *Coatings*, vol. 11, no. 6, p. 684, 2021.

[23] Z. Khan, H. U. Rasheed, I. Tlili, I. Khan, and T. Abbas, "Runge-Kutta 4th-order method analysis for viscoelastic Oldroyd 8-constant fluid used as coating material for wire with temperature dependent viscosity," *Scientific Reports*, vol. 8, no. 1, Article ID 14504, 2018.

[24] H. Ur Rasheed, A. AL-Zubaidi, S. Islam, S. Saleem, Z. Khan, and W. Khan, "Effects of Joule heating and viscous dissipation on magnetohydrodynamic boundary layer flow of Jeffrey nanofluid over a vertically stretching cylinder," *Coatings*, vol. 11, no. 3, p. 353, 2021.

[25] Z. Khan, M. Khan, S. Islam et al., "Analysis of magneto-hydrodynamics flow and heat transfer of a viscoelastic fluid through porous medium in wire coating analysis," *Mathematics*, vol. 5, no. 2, p. 27, 2017.

[26] S. Z. Abbas, W. A. Khan, H. Sun, M. Irfan, M. I. Khan, and M. Waqas, "Von Kármán swirling analysis for modeling Oldroyd-B nanofluid considering cubic autocatalysis," *Physica Scripta*, vol. 95, no. 1, Article ID 015206, 2019.

[27] Z. Khan, W. A. Khan, H. Ur Rasheed, and K. S. Nisar, "Melting flow in wire coating of a third grade fluid over a die using Reynolds' and vogel's models with non-linear thermal radiation and Joule heating," *Materials*, vol. 12, no. 19, p. 3074, 2019.

[28] M. Subhas Abel, J. V. Tawade, and J. N. Shinde, "The effects of MHD flow and heat transfer for the UCM fluid over a stretching surface in presence of thermal radiation," *Advances in Mathematical Physics*, vol. 21, 2012.

[29] N. Vishnu Ganesh, B. Ganga, and A. K. Abdul Hakeem, "Lie symmetry group analysis of magnetic field effects on free convective flow of a nanofluid over a semi-infinite stretching sheet," *Journal of the Egyptian Mathematical Society*, vol. 22, no. 2, pp. 304–310, 2014.

[30] S. Das, H. K. Mandal, R. N. Jana, and O. D. Makinde, "Magneto-nanofluid flow past an impulsively started porous flat plate in a rotating frame," *Journal of Nanofluids*, vol. 4, no. 2, pp. 167–175, 2015.

[31] S. M. Ibrahim, P. V. Kumar, G. Lorenzini, E. Lorenzini, and F. Mabood, "Numerical study of the onset of chemical reaction and heat source on dissipative MHD stagnation point flow of Casson nanofluid over a nonlinear stretching sheet with velocity slip and convective boundary conditions," *Journal of Engineering Thermophysics*, vol. 26, no. 2, pp. 256–271, 2017.

[32] K. A. Kumar, J. V. R. Reddy, V. Sugunamma, and N. Sandeep, "MHD flow of chemically reacting Williamson fluid over a curved/flat surface with variable heat source/sink," *International Journal of Fluid Mechanics Research*, vol. 46, no. 5, pp. 407–425, 2019.

[33] K. Das and L. Zheng, "Melting effects on the stagnation point flow of a Jeffrey fluid in the presence of magnetic field," *Heat Transfer Research*, vol. 44, no. 6, pp. 493–506, 2013.

[34] M. Abd El-Aziz and A. A. Afify, "Influences of slip velocity and induced magnetic field on MHD stagnation-point flow and heat transfer of Casson fluid over a stretching sheet," *Hindawi Mathematical Problems in Engineering*, vol. 23, p. 11, 2018.

[35] S. Z. Abbas, W. A. Khan, M. M. Gulzar, T. Hayt, M. Waqas, and Z. Asghar, "Magnetic field influence in three-dimensional rotating micropolar nanoliquid with convective conditions," *Computer Methods and Programs in Biomedicine*, vol. 189, 2020, Article ID 105324, https://doi.org/10.1016/j.cmpb.2020.105324.

[36] S. J. Liao, *Homotopy Analysis Method in Nonlinear Differential Equations*, Springer & Higher Education Press Heidelberg., Shanghai, China, 2012.

[37] S. Liao, *Beyond Perturbation: Introduction to the Homotopy Analysis Method*, Chapman & Hall/CRC, Boca Raton, FL, USA, 2003.

[38] S. Liao, "An optimal homotopy-analysis approach for strongly nonlinear differential equations," *Communications in Nonlinear Science and Numerical Simulation*, vol. 15, no. 8, pp. 2003–2016, 2010.

[39] R. Naz, "Featuring the radiative transmission of energy in viscoelastic nanofluid with swimming microorganisms," *International Communications in Heat and Mass Transfer*, vol. 117, Article ID 104788, 2020.

[40] R. Naz, M. Noor, M. Javed, and T. Hayat, "A numerical and analytical approach for exploration of entropy generation in Sisko nanofluid flow having swimming microorganisms," *Journal of Thermal Analysis and Calorimetry*, vol. 144, no. 3, pp. 805–820, 2021.

[41] Y. Su, X. Jiang, and Z. Lin, "Simulation and relationship strength: characteristics of knowledge flows among subjects in a regional innovation system," *Science, Technology and Society*, vol. 26, no. 3, pp. 459–481, 2021.